

Low-Dose TOF-PET Based on Surface Electron Production in Dielectric Laminar MCPs

Kepler Domurat-Sousa, Cameron Poe, Henry J. Frisch
Enrico Fermi Institute, University of Chicago

Bernhard W. Adams
Quantum Optics Applied Research

Camden Ertley
SouthWest Research Institute

Neal Sullivan
Angstrom Research, Inc

Published in Nuclear Instruments and Methods, Section A

Abstract

We present simulations of whole-body low-dose time-of-flight positron emission tomography (TOF-PET) based on the direct surface production [1] by 511 keV gamma rays of energetic electrons via the Photo-electric and Compton Effects, eliminating the scintillator and photodetector sub-systems in PET scanners. In Ref. [1] we described Microchannel Plates (MCP) constructed from thin dielectric laminae containing heavy nuclei such as lead or tungsten (LMCPTM). The laminae surfaces are micro-patterned to form channels, which can then be functionalized to support secondary electron emission in the manner of conventional MCPs. After assembly of the laminae, the channels form the pores of the conversion LMCP. This conversion stage is then followed by a high-gain MCP-based amplification stage, which also can be constructed using the laminar technique, but with pores typical of currently-available large-area MCPs .

We have simulated direct conversion using modifications to the TOPAS Geant4-based tool kit. A $20 \times 20 \times 2.54$ cm³ LMCP, composed of 150-micron thick lead-glass laminae, is predicted to have a $\geq 30\%$ conversion efficiency to a primary electron that penetrates an interior wall of a pore. The subsequent secondary electron shower is largely confined to one pore and can provide high space and time resolutions.

In whole-body PET scanners the technique eliminates the scintillator and photodetector subsystems. The consequent absence of a photocathode allows assembly of large arrays at atmospheric pressure and less stringent vacuum requirements, including use of pumped and cycled systems.

TOPAS simulations of the Derenzo and XCAT-brain phantoms are presented with dose reductions of factors of 100 and 1000 from a literature benchmark. New applications of PET at a significantly lower radiation dose include routine screening for early detection of pathologies, the use in diagnostics in previously unserved patient populations such as children, and a larger installed facility base in rural and under-served populations, where simpler gamma detectors and lower radiation doses may enable small low-cost portable PET scanners.

1 Introduction

Positron emission tomography (PET) uses radioactive positron-emitting tracers to locate areas of high biological activity such as tumors and hair-line fractures of bones. It complements other modalities that identify morphologies, and is often used in conjunction with CT or MRI. In addition PET is used on small animals for development of pharmaceuticals and treatments.

In the last decade detectors and techniques for time-of-flight positron emission tomography (TOF-PET) have substantially grown in sophistication [2, 3, 4]. Among other innovations, high-precision whole-body scanners have been built and characterized [5, 6]; TOF-PET with sub-nanosecond coincidence has recently been developed [7]; an international competition to develop sub-10 ps TOF resolution is now in place [8, 9]; and timing with resolutions of 10 ps or below using Cherenkov light in pre-radiators [10, 11, 12] is being developed by Cherry et al. for higher spatial resolutions and lower doses [13].

Recently, alternative methods have been proposed [14, 15, 16, 17] with the goal of achieving resolutions set by the underlying physics processes rather than by the detector segmentation [18]. The technique, which like the conventional technique uses the conversion of the gamma rays in a scintillator followed by photo-detection, is to exploit Compton Scattering of the gamma rays in low atomic number (Z) scintillating media. Successive Compton scatters are constrained by the two-body Compton kinematics, allowing precisely locating the first scatter in a large fraction of events [16, 17].

With similar motivation, here we have adapted the TOPAS Geant4-based framework [19, 20, 21] to study direct surface conversion of gamma rays to electrons via the Compton and Photoelectric effects in MCPs constructed from thin micro-patterned laminae (LMCPTM) containing heavy nuclei such as lead or tungsten [1]. The direct conversion technique eliminates the scintillator and photodetector subsystems in TOF-PET scanners, converting the gamma ray to an electron shower inside an MCP-based planar vacuum tube, the High-resolution Gamma Multiplier Tube (HGMTTM). In addition to the savings in cost, complexity, and bulk from not using heavy crystals and photodetectors, the absence of a photocathode allows assembly of large arrays at atmospheric pressure and much relaxed vacuum requirements, including use of pumped and cycled systems.

The organization of the paper is as follows. Section 2 introduces the HGMT and its components. Section 3 presents gamma ray conversion efficiencies and resolutions from TOPAS simulations of the LMCP. Section 4 presents images from simulations of the Derenzo [22] and XCAT-brain [23] phantoms in a whole-body HGMT-based TOF-PET detector at reduced dose. Portable and animal TOF-PET scanners are discussed in Section 5. Section 6 summarizes the results of this first software study and recommends starting to build and test LMCP/HGMT prototypes. Appendix A discusses future studies of time resolution that are beyond the current scope.

2 The High-resolution Gamma Multiplier Tube (HGMTTM)

The HGMT is a large-area ($\geq 100 \text{ cm}^2$), high-gain ($10^6 - 5 \times 10^7$), low-noise MCP-based electron multiplier vacuum tube, designed to provide correlated high-resolution space/time measurements of gamma rays via the technique of surface direct conversion [1]. The HGMT consists of two stages: a conversion stage in which gamma rays interact near a substrate surface with high-Z nuclei to produce ‘primary’ electrons, followed by a high-gain electron amplification stage with high spatial and time resolution. The implementation of the conversion stage is described here using microchannel plates (MCP) constructed by stacking thin patterned laminae (LMCP) [1]. The amplification stage can be constructed with LMCPs or conventional MCPs, or can be integrated towards the downstream end of the pores of the conversion LMCP, for example.

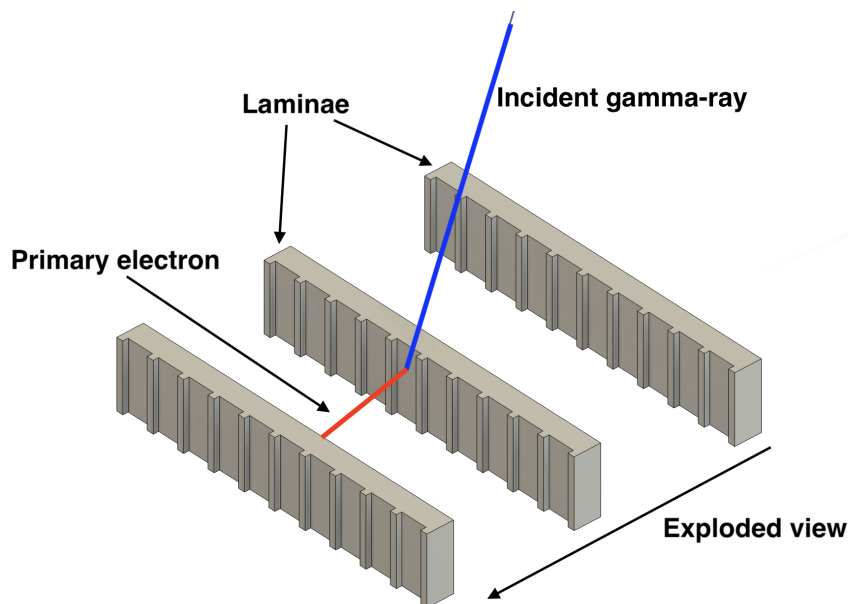


Figure 1: The principle of Surface Direct Conversion [1], in which the gamma ray directly converts to an electron near a surface of an MCP substrate formed from thin laminae (LMCP) containing high-Z nuclei. Three lamina of the LMCP are shown, with purely-illustrative straight rectangular pores (not to scale). This ‘primary’ electron crosses the functionalized surfaces of a pore, producing secondary electrons in the pore.

Figure 1 illustrates the technique. For a 511 keV gamma ray, the primary electron has a short range, and must be produced close to a surface to be detected; the range, typically on the order of a hundred microns in Pb-glass, determines the thickness of the pore walls. The figure illustrates the process for an implementation of the HGMT with LMCPs. The dimensions are not to scale; also the pore geometry and the surface resistive, insulating, and metal coatings, shown here as uniformly resistive, can be tailored to provide local well-defined strike surfaces and high-gain acceleration or low-field drift sections, for example [1].

2.1 The Laminar Micro-Channel Plate (LMCP)

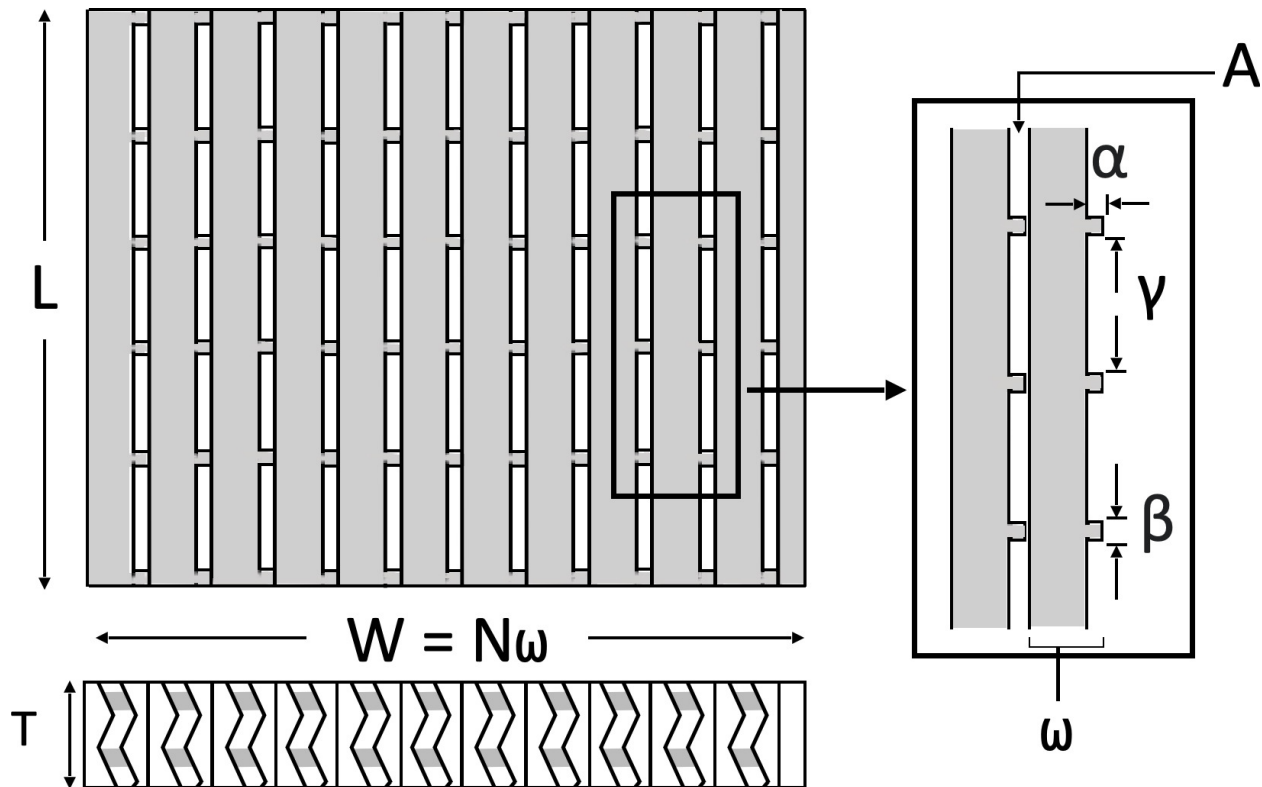


Figure 2: A simplified example of an LMCP body intended for gamma ray detection. The thickness of the body is equal to the width of a lamina, T . Laminae are stacked on edge such that the ridges form pores between the lamina of dimension α perpendicular to the laminate and γ along the laminate surface (see the right-hand inset). The pattern of the pore is purely for illustration.

The LMCP, which is a Micro-Channel Plate (MCP) constructed from thin laminae, is described in detail in Ref. [1]. Figure 2 shows an example of an LMCP body made from a heavy-metal dielectric such as lead-glass [1]. The bulk laminae, which represent the largest fraction of the area of the LMCP, serve to convert the incoming gamma ray to an electron. The patterning and coating of the open-face laminae surfaces before assembly allow optimizations in the pore transverse and longitudinal shapes, variable longitudinal resistance, voltages between strikes, and pore entrance and exit geometries.¹

2.2 The HGMT Components

Figure 3 shows a sketch of a detector assembly of two LMCPs formed with laminae that form structured pores [1]. The open-area ratio (OAR) of the converter LMCP is by design small to maximize the area presented to gamma rays for direct conversion to electrons. The path

¹As described in Ref. [1], a funnel entrance can provide an OAR close to 100% for an amplification LMCP with 5-10 μm patterned pores.

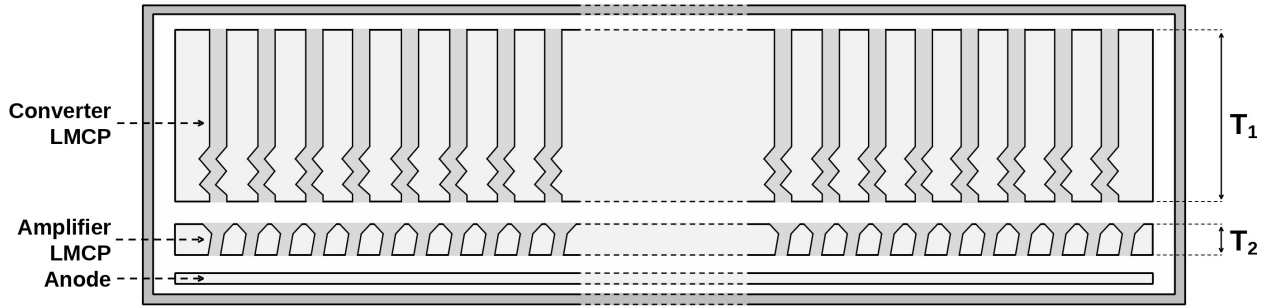


Figure 3: An example HGMT detector assembly with a conversion LMCP, an amplifier LMCP [1], and a multi-channel anode. Gamma rays are incident from above. Note the aspect ratio of the image is distorted by the elision of the center of the tube.

length of the gamma rays in the substrate material depends on the OAR, the thickness and structure of the laminae, and the incident angles of the gamma ray from the normal. The amplification stage, either an LMCP or a conventional MCP, can be made from light glass, and typically will have pores with diameters of 5-40 μm and a length-to-diameter (L/D) ratio of 60-80. The LMCP assembly is followed by an application-specific high-bandwidth anode with sub-mm resolution for readout [24, 25, 26]. Multiple LMCP/anode assemblies can be stacked vertically or horizontally in a common vacuum vessel.

2.3 Anode Configurations

The multi-channel anode records position and time-of-arrival of the electron shower after amplification. There are a number of options for the shape, size, and electrical characteristics of each anode element (e.g. strip, pad) of a patterned anode depending on the application. For low-rate environments such as low-dose TOF-PET² there is extensive experience with anodes with 50-ohm striplines that give sub-mm resolution in both transverse directions [24, 25, 27, 28, 29]. For large-area detectors, such as at a particle collider, arrays of 2-dimensional pads patterned to enhance charge sharing may provide better resolution than rectangular pads, allowing a large decrease in electronic channel count while maintaining the same spatial resolution [26]. For decoupling the anode design from the tube design, as would be economical for mass production of single-design HGMT modules for different uses, an option is capacitive-coupling through an adequately resistive bottom plate for both stripline and pad anodes [30]. Additionally, anodes can be made from solid-state devices.

2.4 Vacuum and Hermetic Packaging

The left-hand panel of Figure 4 represents a 5-by-5 array of HGMTs in a common planar vacuum package such as might be used in a rare kaon decay experiment or at high rapidity in a collider experiment. For 20 cm (8")-square modules the array covers approximately 1 m^2 . Strip-line anodes with sub-mm resolution may be shared across the full extent [31], lowering

²We note that pile-up of gamma rays from multiple e^+e^- annihilations has a quadratic dependence on rate; a dose reduction of a factor of 10^2 reduces pile-up by a factor of 10^4 .

the electronics channel count if rates allow. The right-hand panel is an axial sketch of a PET-scanner array comprised of planar³ LMCP modules that replace the scintillator and photo-detector systems. Multiple modules, including up to the complete array, can share a vacuum vessel.

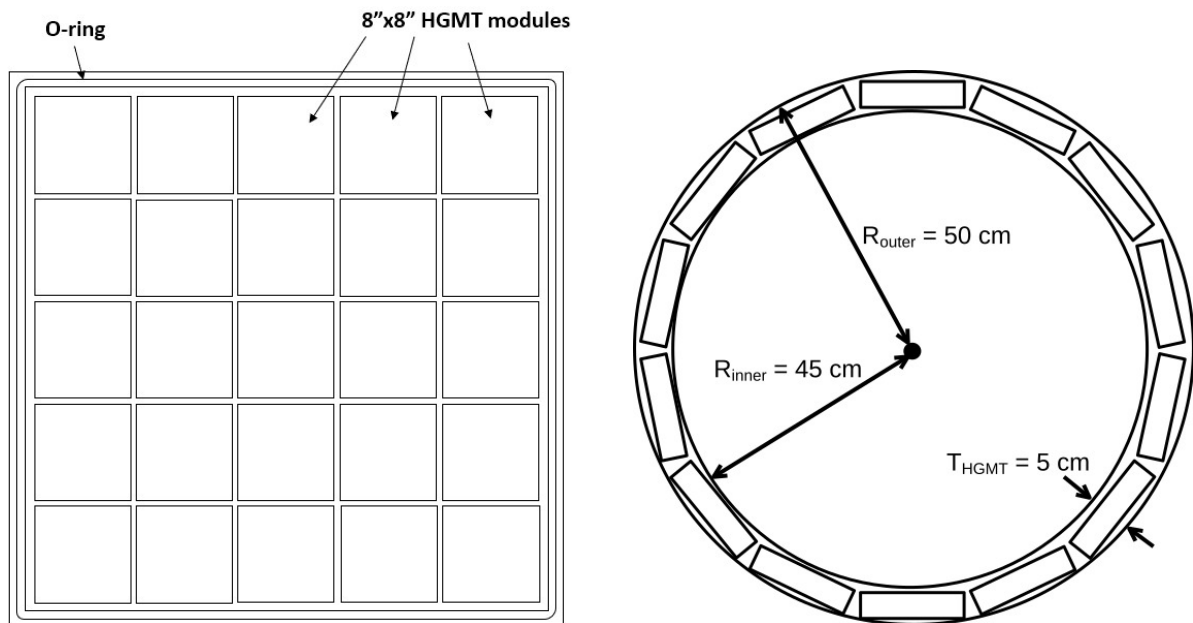


Figure 4: Left: A 5-by-5 array of HGMTs such as would be used in a pre-converter in a particle physics experiment in a common planar vacuum package. Right: An axial view of a whole-body PET-TOF scanner with planar HGMT modules in a common cylindrical vacuum vessel.

The LMCP construction allows wide flexibility in shape and materials for the vacuum package. For gamma rays the tube body can be metal as well as the conventional glass or ceramic. The package may be non-rectangular or non-planar to fit non-standard shaped LMCPs [1]. Appropriately spaced tabs on the perimeter of the laminae can provide support against atmospheric pressure from top to bottom of the tube. As the HGMT has no photocathode, vacuum sealing can be done at atmospheric pressure, with a higher target pressure. Sealing with O-rings, active pumping, and cycling to atmospheric pressure for maintenance or transport become options.

Large systems of HGMTs may be installed in a single vessel such as a cylindrical vessel with an open bore for a PET subsystem, or a large planar vacuum vessel for a photon/electron pre-sampler in a particle physics experiment. For some applications, such as in a large particle collider experiment or inside the magnet bore in a multi-modality PET detector, the HGMT thin aspect ratio saves expensive real-estate over crystal-based gamma ray detection systems. Common packaging also enables a higher packing fraction and economies of shared subsystems. Large systems can be continuously pumped rather than sealed, and can be brought up to atmospheric pressure for maintenance or modification.

³In practice these would most likely be sections of a cylinder [1].

3 Simulation Results: Conversion Efficiencies and Space and Time Resolutions

The analyses of the efficiencies and resolutions of the HGMT were carried out using simulations performed with TOPAS [20], a user-friendly interface for the Geant4 simulation package of the interaction of particles with matter [32, 33]. The simulations of gamma rays, positrons, and electrons used the Geant4 physics lists “G4EMStandardPhysics_option4” and “G4EmPenelopePhysics” [34]. The substrate material for the HGMT was set as the internal Geant4 material “G4_GLASS_LEAD”.

TOPAS has previously been shown to replicate the positron range and distribution of positron energies at annihilation of TOF-PET [16, 19] and serve as a reliable simulation of other types of medical imaging procedures [35, 36, 37].

3.1 Gamma Ray Conversion Efficiency

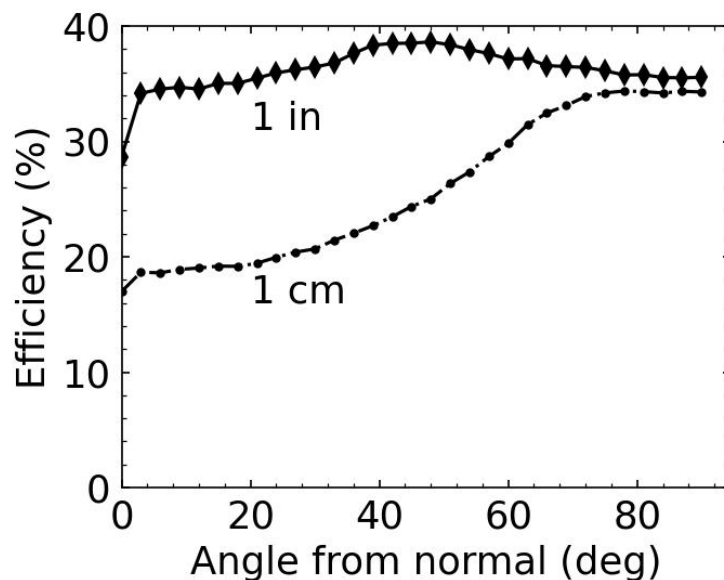


Figure 5: The efficiency for direct conversion of a 511 keV gamma ray versus incident angle from the normal. Distributions are shown for LMCP thicknesses of 1 cm and 2.54 cm (1 inch) with a lead-glass (“G4_GLASS_LEAD”) substrate.

Figure 5 displays the efficiency for MCP thicknesses of 1 cm and 2.54 cm (1 inch) found in the TOPAS simulation for direct conversion of a 511 keV gamma ray versus incident angle from the normal to the lamina. The efficiency includes the creation of a primary electron that enters a pore by crossing a functionalized pore-defining wall.

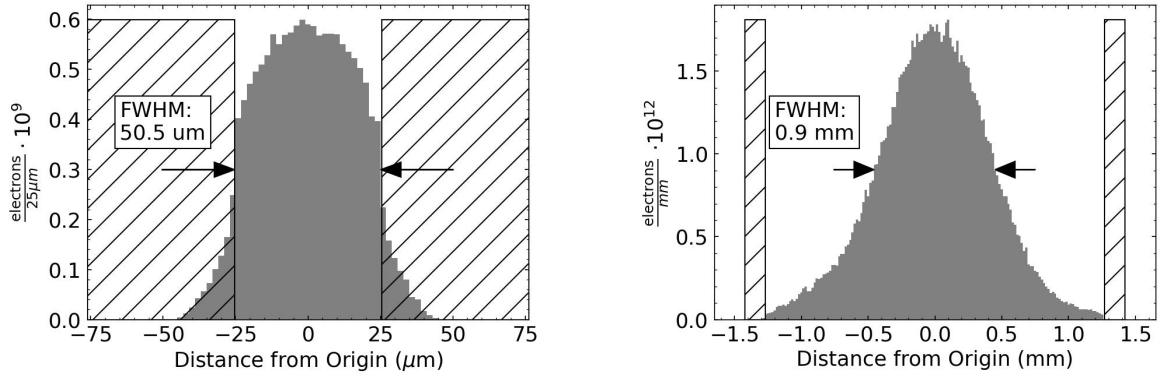


Figure 6: The one-dimensional spatial distributions, in the ‘short’ and ‘long’ dimensions, of charge at the exit of a 50 micron by 2.5 mm rectangular pore as shown in Figure 2. The pore walls are indicated by hatching. The distributions are from a TOPAS simulation of a single secondary electron created on the ‘short’-dimension wall, 7.5 mm from the pore exit.

3.2 Spatial Resolution

Figure 6 shows the simulated spatial distributions in the ‘short’ and ‘long’ dimensions of charge generated by a single secondary electron created on the ‘short’-dimension wall, 7.5 mm from the pore exit. The pore has a uniform profile with transverse dimensions of 50 μm by 2.5 mm.⁴ The TOPAS simulation of secondary emission and multiplication is initiated at the point of a primary electron on the wall of the pore (left-hand surface in the Figure). The hatched regions represent the substrate walls between neighboring pores.

3.3 Time Resolution

The simulation of the time resolution of an HGMT depends on the choice of many parameters of the HGMT construction, including details of the materials and shapes of the pore-forming surfaces, and consequently is beyond the scope of our simulations. Data from a physical LMCP are essential in narrowing the options towards high-resolution and robustness. In consequence, in the simulations of imaging presented in Section 4 we have used a parametric approach, setting the time resolution in the simulation to 100 ps independent of the position of the gamma ray conversion in the pore. Appendix A presents images simulated at different resolutions, including one using no TOF information, and discusses possible future strategies for lowering the spread in times due to the variation in conversion point to below 100 ps.

⁴Here we have chosen to display an atypically large value for one dimension to demonstrate the effect. The size of the pores in an HGMT will most likely be in the tens of microns or less in both dimensions.

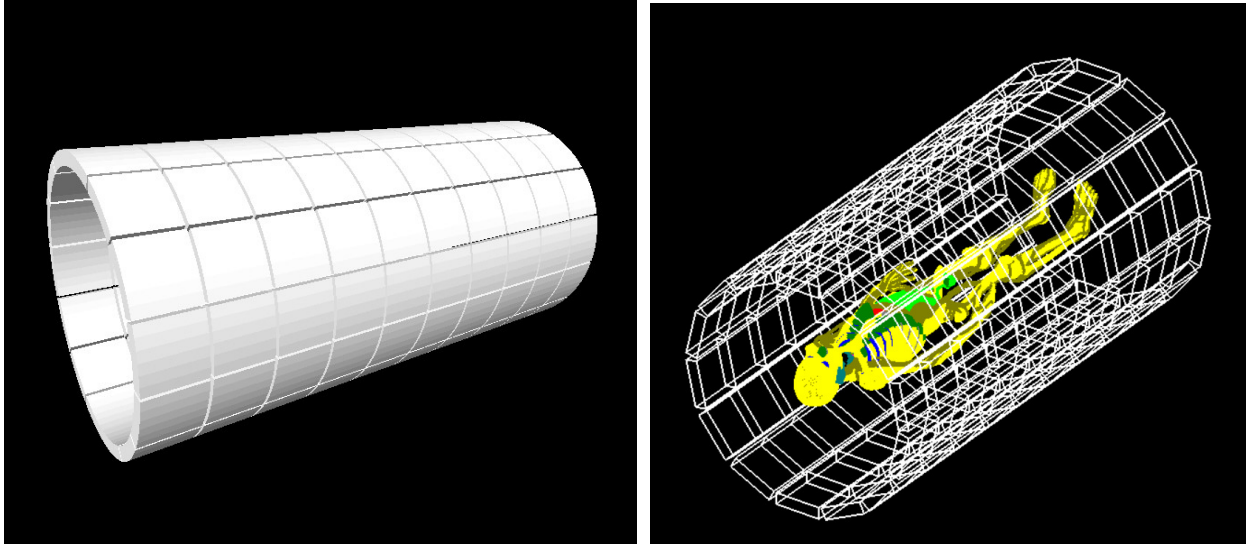


Figure 7: Left: A schematic whole-body PET scanner based on curved HGMT modules. Right: the graphical rendition of the whole-body scanner based on rectangular HGMTs including the XCAT phantom used in the TOF-PET simulation. The scanner is 200 cm long and has a bore radius of 45 cm.

4 Simulation of a Whole-Body HGMT TOF-PET Scanner

4.1 Whole-Body Scanner Configuration

The left-hand panel of Figure 7 shows a representative whole-Body TOF-PET scanner made with curved [1] HGMT modules. The scanner benefits from the absence of a layer of scintillator to convert the gamma rays to optical photons, and the absence of the corresponding photodetector system to convert the optical photons to electrons. The right-hand panel shows the XCAT phantom inside the scanner as simulated in TOPAS. The scanner is 200 cm long and has a bore radius of 45 cm.

As the detector typically would be ≈ 5 cm thick in the radial direction, the HGMT facilitates integration into multi-modality systems such as PET/MRI and PET/CT. The absence of the scintillator and photodetector systems also substantially reduces complexity.

4.2 Simulation of the Derenzo Phantom at Reduced Doses

Figures 8 and 9 show reconstructed images of the Derenzo phantom [22] at 1/100th and 1/1,000th reduced doses from a benchmark dose of 15 kBq/mL for the rods and 5 kBq/mL for the background at a scan time of 10 minutes. The timing resolution was taken as 100 ps (FWHM); the spatial resolution in the plane of the LMCP at the pore exit was conservatively set to 1 mm in both the ‘long’ and ‘short’ dimensions.

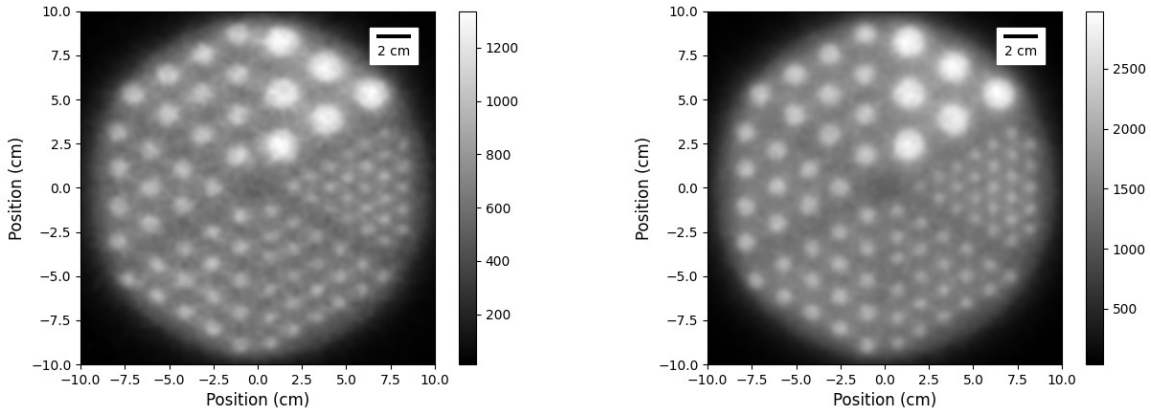


Figure 8: Reconstructed images of the Derenzo phantom at a dose of 150 Bq/mL for the rods and 50 Bq/mL for the background, a factor of 100 lower than the benchmark dose. The thickness of the converter LMCP is 1 cm in the left-hand image, and 2.54 cm (1 inch) in the right-hand image.

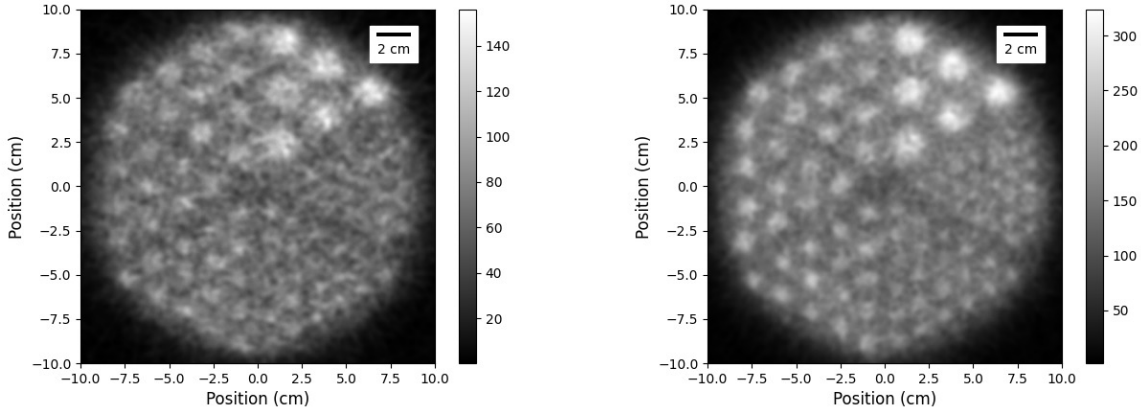


Figure 9: Reconstructed images of the Derenzo phantom at a dose of 15 Bq/mL for the rods and 5 Bq/mL for the background, a factor of 1000 lower than the benchmark dose. The thickness of the converter LMCP is 1 cm in the left-hand image, and 2.54 cm (1 inch) in the right-hand image.

4.3 Simulation of the XCAT Brain Phantom and 2 cm-Diameter Lesion at Reduced Doses

The XCAT brain phantom [23] was also simulated at 1/100th, 1/1,000th, and 1/10,000th reduced doses from a benchmark dose of 8.25 kBq/mL for white matter, 33 kBq/mL for gray matter, and 99 kBq/mL for the spherical lesion [38] for an estimated 10-minute scan. Figures 10, 11, and 12 show the brain at these doses, respectively. While the images at 1/10,000th dose are not good enough for detailed diagnosis, they may be enough to suggest a follow-up scan at a higher dose, and may inform strategies for regular screening of appropriate

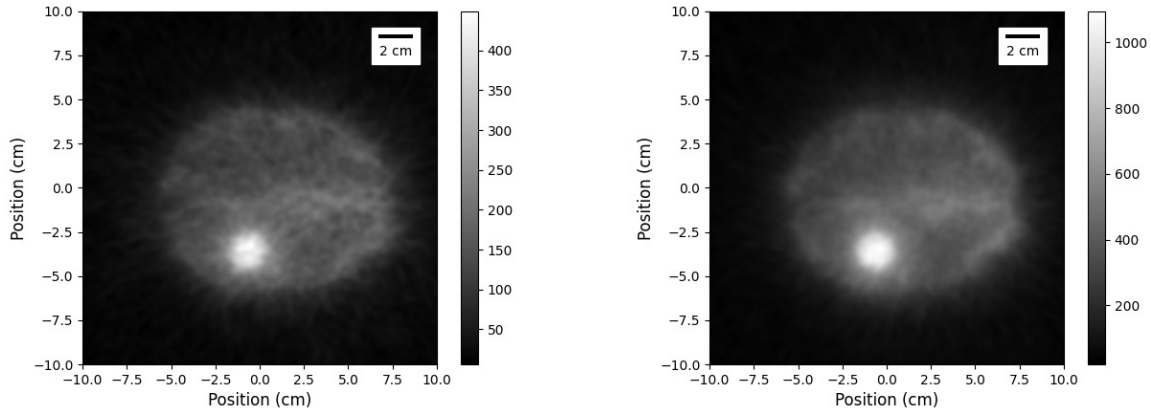


Figure 10: Reconstructed images of the XCAT brain phantom with a 2 cm-diameter spherical lesion at a dose reduced by a factor of 100 from the benchmark [38]: 82.5 Bq/mL for white matter, 330 Bq/mL for gray matter, and 990 Bq/mL for the lesion. The thickness of the converter LMCP is 1 cm in the left-hand image, and 2.54 cm (1 inch) in the right-hand image.

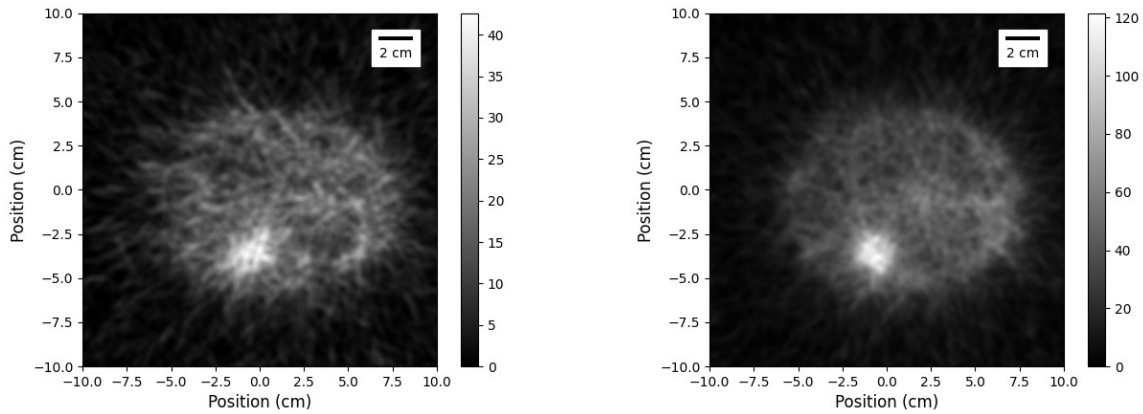


Figure 11: Reconstructed images of the XCAT brain phantom with a 2 cm-diameter spherical lesion at a dose reduced by a factor of 1000 from the benchmark [38]: 8.25 Bq/mL for white matter, 33 Bq/mL for gray matter, and 99 Bq/mL for the lesion. The thickness of the converter LMCP is 1 cm in the left-hand image, and 2.54 cm (1 inch) in the right-hand image.

populations, such as selective annual exams for breast cancer.

5 Portable and Animal TOF-PET Scanners

A significantly lower dose may allow the use of portable TOF-PET scanners for clinical applications and facilities for which PET is not currently possible or economical. Examples

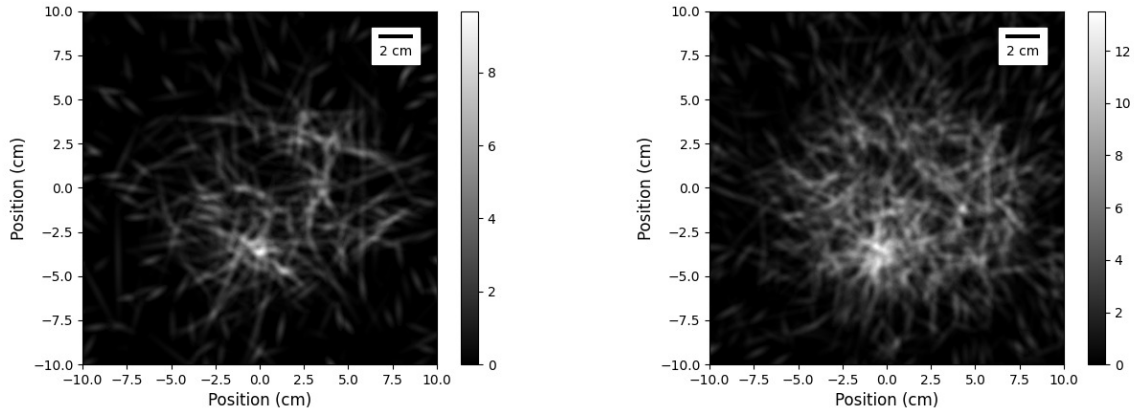


Figure 12: Reconstructed images of the XCAT brain phantom with a 2 cm-diameter spherical lesion at a dose reduced by a factor of 10,000 from the benchmark [38]: 0.825 Bq/mL for white matter, 3.3 Bq/mL for gray matter, and 9.9 Bq/mL for the lesion. The thickness of the converter LMCP is 1 cm in the left-hand image, and 2.54 cm (1 inch) in the right-hand image.

Portable Limb PET Scanner

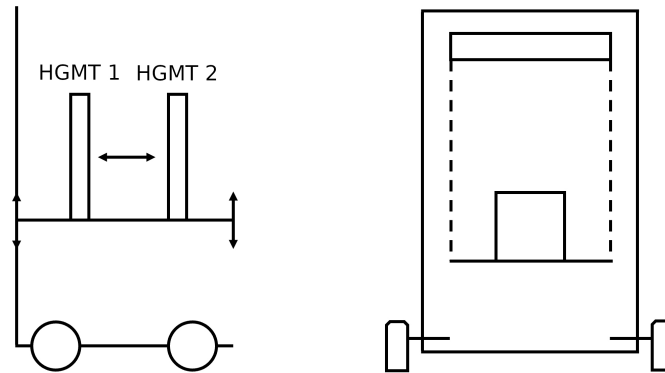


Figure 13: A schematic portable PET scanner based on HGMT modules. The scanner comprises several HGMTs. The HGMTs can be sealed or pumped by a small pump on the cart. The HGMTs can sit on a stage adjustable in height and aperture for imaging breaks in arms or legs, for example. Local electronics and computation can give a real-time image.

are hair-line fractures, for which the current standard of X-rays has a significant rate of non-detection [39], but for which PET has high sensitivity. Figure 13 shows a sketch of a simple two-module portable scanner on a portable cart that can be adjusted in height and aperture to accommodate legs and arms, for example. Because the HGMT does not have a photocathode, it does not need ultra-high vacuum (UHV), and can be pumped with a small vacuum pump located on the cart. The system can be valved off, transported, and restarted at a new location.

Figure 14 shows a representative PET scanner for small animals. The large area of

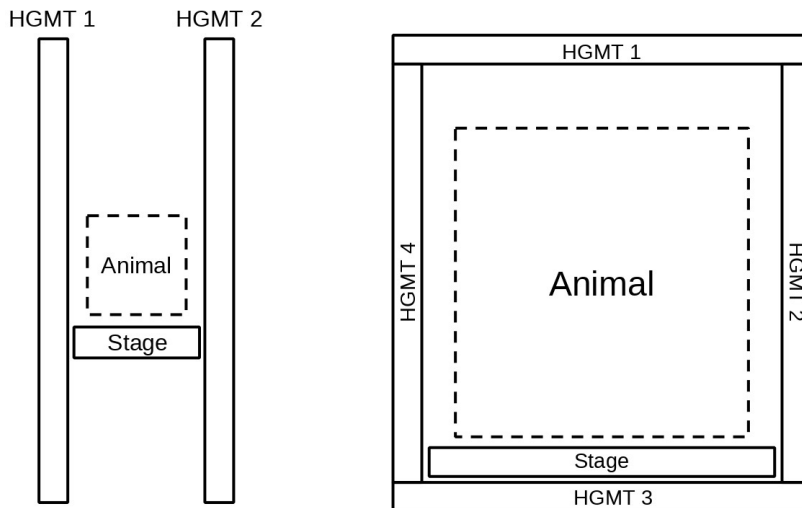


Figure 14: Left: A schematic economical small-animal PET scanner formed by two HGMT modules. Right: A small-animal PET scanner formed by four modules in azimuth.

the HGMT may allow coverage of much of the solid angle with only two HGMTs. An array of multiple HGMTs covering four or six sides can provide coverage for larger animals.

6 Summary and Conclusions

We have adapted the TOPAS Geant4-based tool kit to simulate surface direct conversion in a Laminated Micro-Channel Plate (LMCP) constructed from thin lead-glass laminae 150 microns-thick [1]. An LMCP 2.54 cm-deep is predicted to have a $\geq 30\%$ conversion efficiency to a primary electron that penetrates an interior wall of a pore. We present space and time resolutions from the subsequent secondary electron shower. Images from initial simulations of whole-body HGMT TOF-PET scanners at doses reduced from literature benchmarks by factors of 100 and 1000 are presented.

In whole-body PET scanners the technique eliminates the scintillator and photodetector subsystems. In addition, the absence of a photocathode eliminates many onerous aspects of current UHV fabrication, as it allows assembly of large arrays at atmospheric pressure with less stringent vacuum requirements, including use of pumped and cycled systems.

TOPAS simulations of the Derenzo and XCAT-brain phantoms are presented with dose reductions of factors of 100 and 1000 from literature benchmarks. Benefits of such reduction would include routine screening for early tumor detection, use of PET for pediatric diagnostics, and a larger installed facility base in rural and under-served populations.

Application-specific implementations of the surface direct production technique employed in the HGMT are also candidates for large-area arrays for use in detectors across a wide range of fields in physics.

In conclusion, initial TOPAS Geant4-based simulation studies of whole-body TOF-PET using direct conversion of the gamma rays to electrons via the Photoelectric and Compton Effects indicate the possibility of useful imaging at substantially lower radiation doses. The LMCP technique of laminated construction of micro-channel plates, in this case with

at least part of each lamina consisting of a material with heavy nuclei such as those of lead or tungsten, would allow access to many operational parameters for detector optimization. We hope others interested in making the unique capabilities of positron emission tomography widely and routinely available will join us in applying resources to building and testing hardware.

7 Appendix A: Time Uncertainty From the Varying Conversion Point

The power of measuring the position of the e^+e^- annihilation as a point in three dimensions, rather than the 2-dimensional Line-of-Response (LOR), represents a reduction of orders-of-magnitude in required radiation dose, as well as a move from image reconstruction to pattern recognition. There are now efforts to achieve a resolution in the longitudinal direction of the LOR comparable to the transverse resolution⁵ of a few mm or less [8, 9, 16]. The studies of signal development and wave-form sampling front-end electronics for the requisite time resolution are quite mature [40, 41] and so the problem devolves to the time-resolution of the detector itself. The dependence of the image on the time-of-flight resolution is illustrated in Figure 15, which shows the simulated image of the XCAT brain at a dose reduced by a factor of 1000 for four different time resolutions (FWHM): 50, 100, 200 ps, and 10 nsec, i.e. a resolution much larger than the scanner.

7.1 Contribution to the Timing Resolution from the Secondary Shower Formation

The contribution to the timing resolution from the secondary shower development will be dominated by the multiplicity early in the shower, in particular the multiplicity of the secondary electrons created by the primary electron crossing the functionalized pore-forming surfaces. The left hand panel in Figure 16 shows a simulated pulse shape from a single secondary electron 7.5 mm from the exit end of the pore and centered on one of the short sides. The right-hand panel presents simulations of showers started from a different multiplicity of secondary electrons. Poisson statistics predicts that a higher multiplicity of initial secondary electrons improves the time resolution as the probability of seeing no electrons in the initial time interval falls exponentially in the expected number per unit time with the length of the interval.⁶ In the simulation of Figure 16, electrons are started one-at-a-time 7.5 mm from the exit of the pore, centered in the short direction between the two walls. Any electron exiting the plane enters the amplifying LMCP(s) below, followed by an anode.

The contribution to the time resolution from the secondary shower in the limit of large first-strike secondary emission, shown in Figure 16, is well below 50 ps. The resolution

⁵We note that 10 ps corresponds to a light travel distance of 3 mm for a single-ended measurement in vacuum.

⁶We call the case in which the system has enough gain that a single electron triggers the system to determining the time ‘First-One-In’.

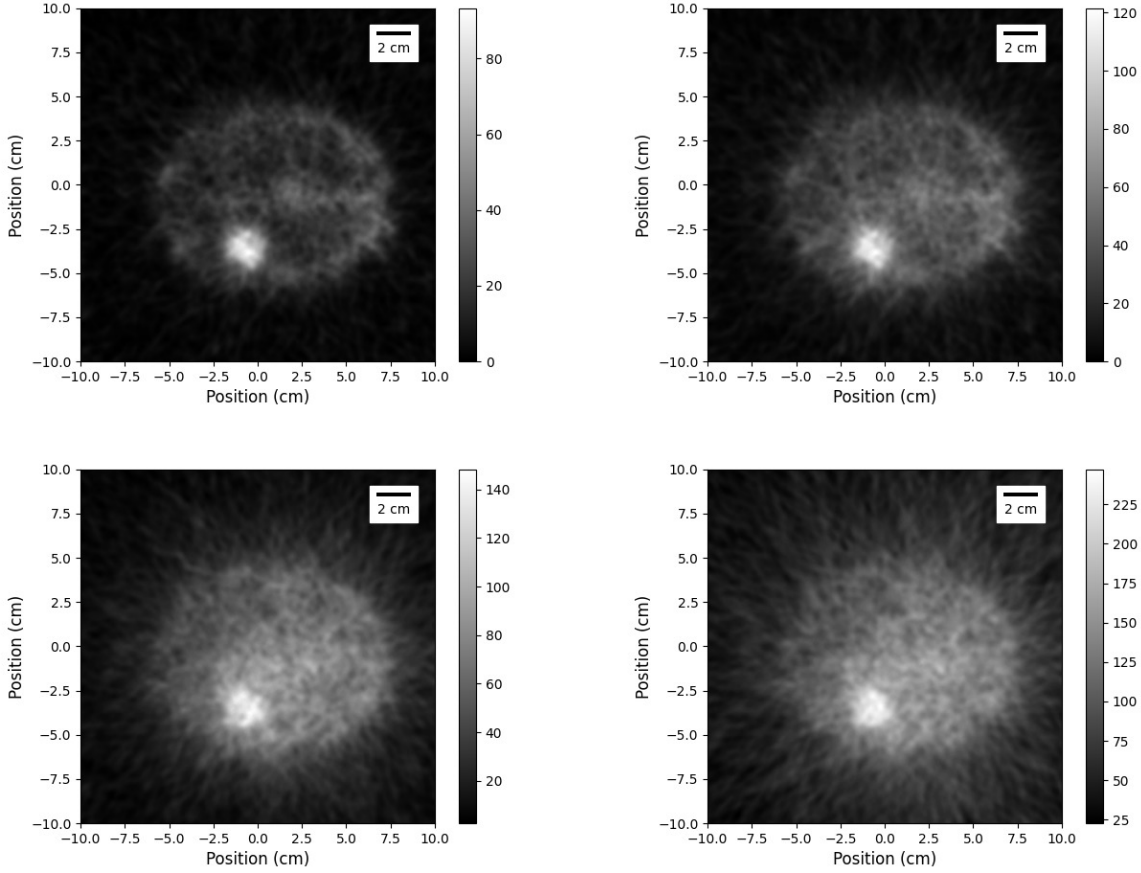


Figure 15: Reconstructed images at different time resolutions of the XCAT brain phantom with a 2 cm-diameter spherical lesion at a dose reduced by a factor of 1000 from the benchmark [38]: 8.25 Bq/mL for white matter, 33 Bq/mL for gray matter, and 99 Bq/mL for the lesion. Top left: Time resolution of 50 ps (FWHM); Top right: Time resolution of 100 ps (FWHM); Bottom left: Time resolution of 200 ps (FWHM); Bottom right: Time resolution of 10,000 ps (FWHM), equivalent to no time cut.

will consequently be dominated by the varying distance of the start of the shower to the pore exit.

7.2 Contribution to the Timing Resolution from the Starting Position Along the Pore

Figure 17 shows the time of arrival of the first secondary electron at the exit plane of the lead-glass converter LMCP versus the height of the initiating point in the pore wall. For a given desired time resolution, the slope determines the maximum thickness in the LMCP of the lead-glass converter section before the conventional MCP amplification section of the HGMT for this contribution not to dominate in the absence of other solutions.

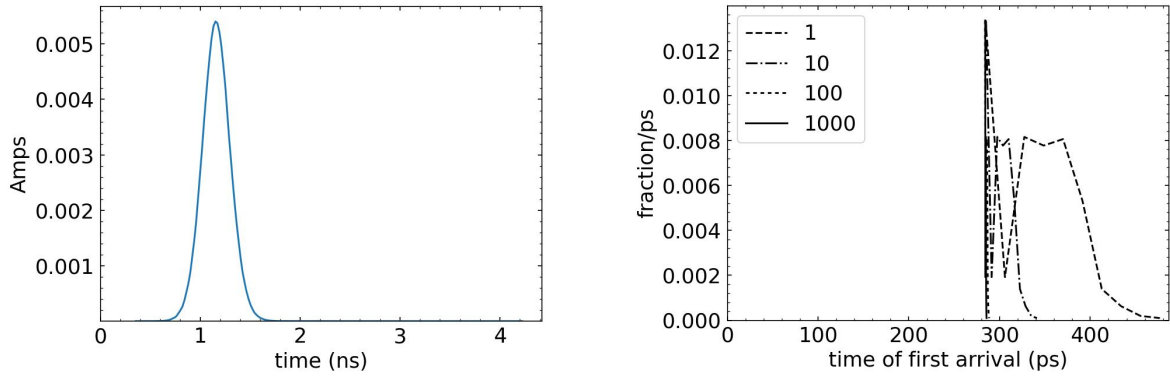


Figure 16: Left: The current predicted by the TOPAS simulation in the secondary electron shower at the pore exit versus time for a cascade initiated by a single secondary electron 7.5 mm from the exit end of the pore and centered on one of the short sides. Right: The time of the first secondary electron that arrives at the exit plane of the lead-glass converter LMCP from a TOPAS simulation of the electron shower in one pore of the LMCP of Figure 2, versus the number of secondary electrons created by the primary electron from the direct gamma conversion.

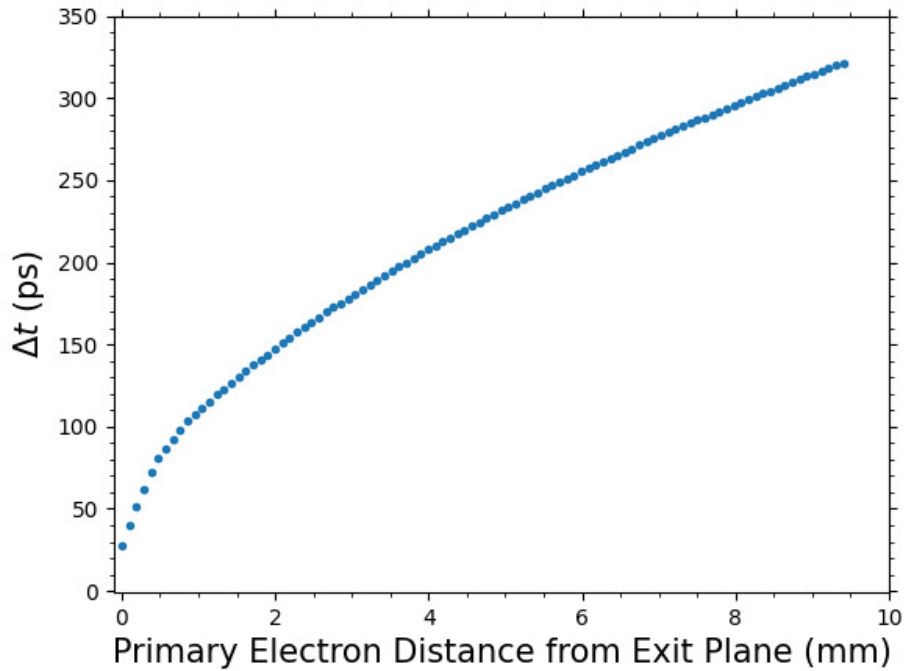


Figure 17: The time of arrival of the first electron at the exit plane versus the height of the initiating point in the LMCP pore wall.

7.3 Can One Overcome the Position Dependence in the LMCP Pore?

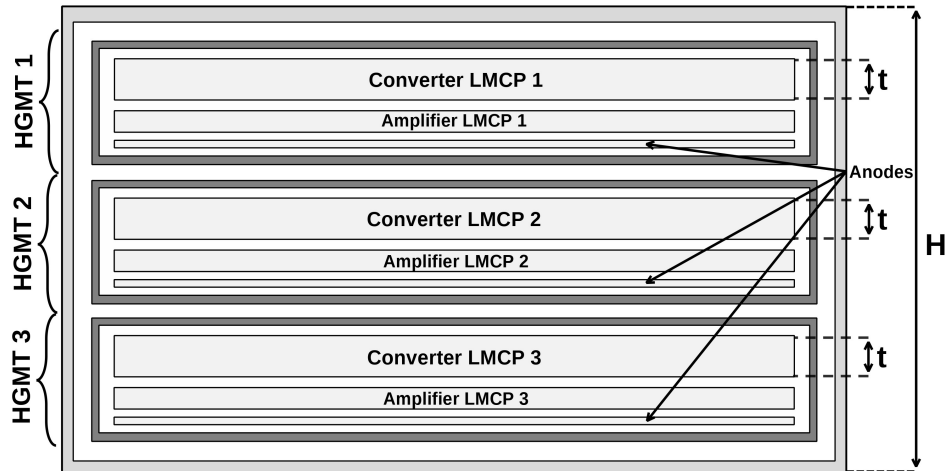


Figure 18: An example of using stacked HGMT internals with thinner conversion LMCPs to lower the uncertainty due to the primary interaction in the pore walls.

One straight-forward strategy to lower the time resolution below 100 ps is to stack multiple HGMT internal modules, each consisting of a converter LMCP made with lead-glass followed by one or more amplification sections made from B33 glass or equivalent, and an anode. A stack of these HGMT sub-modules with a total conversion path length of a several cm will be less expensive and less bulky than conventional crystal systems.⁷ Figure 18 shows an example stack of 3 HGMT assemblies in a common vacuum package. Each of the Conversion LMCP/Amplification LMCP/anode assemblies would provide a conversion path length appropriate for the desired time resolution and overall conversion efficiency. The system cost and bulk are expected to be less than those of conventional crystal-based scintillator systems.

The LMCP technique may support more-sophisticated strategies than the above brute force stacking, and can be explored in a program of measurements of actual devices. For example, the design could enhance the correlation of pulse height with conversion point in the LMCP. A pore design with discrete strike points spaced at small intervals, for example 1 mm, and resistances such that the potential between them is well up on the SEY curve (e.g. at 4 for MgO) [42] will produce some measure of discrete gain versus height from the pore exit. A more speculative example to be explored that illustrates the flexibility of the open-face LMCP construction technique is to incorporate RF pickups at intervals along pores before assembly. The pattern of signals from the antennae along the pore would locate the start of the secondary shower. However the brute force approach of multiple thin LMCP assemblies described above should be feasible and affordable.

⁷Strip-line anodes are constructed from inexpensive two-layer printed circuit boards, and 150 electronics channels can cover a square meter. The sub-modules share a common hermetic package and High Voltage distribution.

Acknowledgments

We thank Joseph Perl and Paul Segars for the exemplary development of TOPAS and XCAT and for their remarkable user support. We are indebted to Mary Heintz for exceptional computational system development and advice. Benjamin Cox provided highly informed encouragement, advice, and support. We are grateful to Ian Goldberg, Justin Gurvitch, and Richmond Yeung for graphics contributions. We deeply thank an anonymous reviewer for thoughtful comments.

K. Domurat-Sousa, and C. Poe were supported by the University of Chicago College, Physical Sciences Division, and Enrico Fermi Institute, for which we thank Steven Balla and Nichole Fazio, Michael Grosse, and Scott Wakely, respectively. C. Poe was additionally supported by the University of Chicago Quad Undergraduate Research Scholars program and the Jeff Metcalf Internship program.

References

- [1] K. Domurat-Sousa, C. Poe, Henry J. Frisch, B. W. Adams, C. Ertley, Neal Sullivan; *Surface Direct Conversion of 511 keV Gamma Rays in Large-Area Laminated Multichannel-Plate Electron Multipliers*; *Nucl. Instrum. Methods*; 2023 1055:168438; <https://doi.org/10.1016/j.nima.2023.168538>
- [2] S. Vandenberghe, P. Moskal, J. S. Karp; *State of the art in total body PET* EJNMMI Phys. 2020 May 25;7(1):35. doi: 10.1186/s40658-020-00290-2.
- [3] J. J. Vaquero and P. Kinahan; *Positron Emission Tomography: Current Challenges and Opportunities for Technological Advances in Clinical and Preclinical Imaging Systems* Annual Review of Biomedical Engineering Volume 17, 385; (2015)
- [4] M. E. Phelps, S. R. Cherry, and M. Dahlbom; *PET: Physics, instrumentation, and scanners*; Springer New York (2006); doi.org/10.1007/0-387-34946-4
- [5] S. Vandenberghe, P. Moskal, J.S. Karp; *State of the art in total body PET*; EJNMMI Phys. 2020 May 25;7(1):35.
- [6] R. D. Badawi, H. Shi, and S. R. Cherry et al. *First Human Imaging Studies with the EXPLORER Total-Body PET Scanner*; J Nucl Med. 2019 Mar; 60(3): 299-303. doi: 10.2967/jnumed.119.226498
- [7] M.S. Lee, J. Cates, A. Gonzalez-Montoro, and C. Levin; *High-resolution time-of-flight PET detector with 100 ps coincidence time resolution using a side-coupled phoswich configuration*; Phys. Med. Biol. in press: <https://doi.org/10.1088/1361-6560/ac01b5> (2021)
- [8] P. Lecoq, C. Morel and J. Prior; *Case for setting up a 10ps challenge: A step toward reconstruction-less TOF-PET*; Nuovo Cim. C **43** (2020) no.1, 2 doi:10.1393/ncc/i2020-20002-y
- [9] P. LeCoq et al.; *Roadmap toward the 10 ps time-of-flight PET challenge*; Physics in Medicine and Biology, Vo. 65, Number 21. Oct, 2020
- [10] T. Credo, H. Frisch, H. Sanders, R. Schroll, and F. Tang; *Picosecond Time-of-Flight Measurement for Colliders Using Cherenkov Light* Proceedings of the IEEE, Rome, Italy, Oct. 2004; Nuclear Science Symposium Conference Record, 2004 IEEE, Vol. 1.
- [11] K. Inami, N. Kishimoto, Y. Enari, M. Nagamine, and T. Ohshima; *A 5-ps Tof-counter with an MCP-PMT*; Nucl. Instr. Meth. A560, p.303, 2006
- [12] A. Ronzhin et al.; *Development of a 10 ps level time of flight system in the Fermilab Test beam facility*; Nucl. Instr. Meth. A623,931(2010).

- [13] R. Ota, S. I. Kwon, E. Berg, F. Hashimoto, K. Nakajima, I. Ogawa, Y. Tamagawa, T. Omura, T. Hasegawa, S. R. Cherry;
Direct positron emission imaging: ultra-fast timing enables reconstruction-free imaging
<https://arxiv.org/ftp/arxiv/papers/2105/2105.05805.pdf>
- [14] E. Spieglan; *Using Switchable Fluorescent Molecules to Image Tracks and Measure Energy in Large Liquid Double Beta Decay Detectors*; CPAD 2019;
<https://agenda.hep.wisc.edu/event/1391/timetable/#20191209.detailed>
- [15] J.F. Shida, E. Spieglan, B.W. Adams, E. Angelico, K. Domurat-Sousa, A. Elagin, H. J. Frisch, P. La Rivière, A. H. Squires; *Ionization-activated Multi-State Low-Z Detector Media Nucl. Inst. and Meth. A*; Vol. 1017; Nov. 2021;
- [16] K. Domurat-Sousa, C. M. Poe, M. S. McDaniel, E. Spieglan, J. F. Shida, E. Angelico, B. W. Adams, P. J. L. Riviere, H. J. Frisch, A. H. Squires;
Simulation of a low-Z-medium detector for low-dose high-resolution TOF-PET
Submitted to IEEE Transactions on Medical Imaging (TMI), May 2023;
arXiv preprint (2023) <https://arxiv.org/abs/2305.07173>
- [17] A. H. Squires, *Detecting Compton Scatters in Liquid Media for Low-Dose High-Resolution TOF-PET*; DOE-NIH Workshop *Advancing Medical Care through Discovery in the Physical Sciences: Radiation Detection* March 16, 2023; Jefferson National Accelerator Facility
- [18] W. W. Moses; *Fundamental Limits of Spatial Resolution in PET*;
Nucl Instrum Methods Phys Res A. 2011 Aug 21;648 Supplement 1:S236-S240. doi: 10.1016/j.nima.2010.11.092.
- [19] K. Domurat-Sousa and C. Poe; *Methods for Simulating TOF-PET in TOPAS Using a Low-Z Medium*; Submitted to Nuclear Instruments and Methods, 2023, 1057:168675, <https://doi.org/10.1016/j.nima.2023.168675>
- [20] B. Faddegon, J. Ramos-Mendez, J. Schuemann, J. Shin, J. Perl, H. Paganetti
The TOPAS tool for particle simulation, a Monte Carlo simulation tool for physics, biology and clinical research
European Journal of Medical Physics; Volume 72, P114-121, April (2020); DOI:<https://doi.org/10.1016/j.ejmp.2020.03.019>
- [21] The TOPAS home page is <https://sites.google.com/a/topasmc.org/home/home>.
Complete user documentation can be found at:
<https://topas.readthedocs.io/en/latest/getting-started/intro.html>
The TOPAS user forum is also available to TOPAS license holders. The low-energy packages Penelope and Option 4 are further described in <https://geant4.web.cern.ch/node/1731>
- [22] S. E. Derenzo; *Monte Carlo simulations of time-of-flight PET with double-ended readout: calibration, coincidence resolving times and statistical lower bounds.*
Phys Med Biol. 2017 May 7;62(9):3828-3858.

- [23] W. P. Segars, G. Sturgeon, S. Mendonca, J. Grimes, B. M. Tsui;
4D XCAT phantom for multimodality imaging research
Med Phys. 2010 Sep;37(9):4902; doi: 10.1118/1.3480985.
- [24] F. Tang, C. Ertley, J.-F. Genat, J. Anderson, K. Byrum, G. Drake, E. May, and G. Sellberg *Transmission-Line Readout with Good Time and Space Resolutions for Planar MCP-PMTs*, in Topical Workshop on Electronics for Particle Physics, CERN, pp. 579-583, 2008
- [25] H. Grabas, R. Obaid, E. Oberla, H. Frisch J.-F. Genat, R. Northrop, F. Tang, D. McGinnis, B. Adams, and M. Wetstein *RF Strip-line Anodes for Psec Large-area MCP-based Photodetectors*, Nucl. Instr. Meth. A71, pp124-131, May 2013
- [26] J. Park, F. Wu, E. Angelico, H. J. Frisch, and E. Spiegler;
Patterned anodes with sub-millimeter spatial resolution for large-area MCP-based photodetector systems;
Nuclear Inst. and Methods in Physics Research, A 985 (2021) 164702; 22 Sept, 2020
- [27] E. Oberla, *Charged Particle Tracking in a Water Cherenkov Optical Time Projection Chamber*, Ph.D Dissertation, University of Chicago, Aug. 2015 The University of Chicago ProQuest Dissertations Publishing, 2015. 3725533.
- [28] E. Oberla and H.J. Frisch; *Charged particle tracking in a water Cherenkov optical time-projection chamber*; Nucl. Inst. Meth. Phys. Res. A814, 19 (April 2016); ISSN 0168-9002; arXiv:1510.00947
- [29] E. Angelico; *Development of Large-Area Mcp-Pmt Photo-Detectors for a Precision Time-Of-Flight System at the Fermilab Test Beam Facility*; Ph.D thesis, The University of Chicago. ProQuest Dissertations Publishing, 2020. 28023552.
- [30] E. Angelico, T. Seiss, B.W. Adams, A. Elagin, H. Frisch, E. Oberla, E. Spiegler;
Capacitively coupled Pulse Readout in a 20cm×20cm MCP-based photodetector Nucl. Instr. Meth. A, 2016
- [31] B.W. Adams, A. Elagin, H. Frisch, R. Obaid, E. Oberla, A. Vostrikov, R. Wagner, J. Wang, M. Wetstein; *Timing Characteristics of Large Area Picosecond Photodetectors*; Nucl. Instr. Meth. Phys. Res. A, Vol. 795, 1 (Sept. 2015).
- [32] S. Agostinelli et al.; *Geant4- A Simulation Toolkit*; Nucl. Instr. Meth. A506, 3, 250; (2003)
- [33] S. Incerti et al.; *Comparison of GEANT4 very low energy cross section models with experimental data in water*;
Medical Physics; 17 August 2010, <https://doi.org/10.1118/1.3476457>
- [34] Physics lists EM constructors in Geant4 10.4,
<http://web.archive.org/web/20230126215656/https://geant4.web.cern.ch/node/1731>,
(accessed on June 16th, 2023).

- [35] Z. Chen, H. Liu, J. Zhao, S. Kaess,
TOPAS Monte Carlo simulation for a scanning proton therapy system in SPHIC;
Journal of Radiation Research and Applied Sciences, Volume 15, 122; (2022).
- [36] Lu, G., Marsh, S., Damet, J. et al.; *Dosimetry in MARS spectral CT: TOPAS Monte Carlo simulations and ion chamber measurements*; Australasian Phys Eng Sci Med 40, 297 (2017). <https://doi.org/10.1007/s13246-017-0532-8>
- [37] A. Bertolet et al, *Pre- and post-treatment image-based dosimetry in ^{90}Y -microsphere radioembolization using the TOPAS Monte Carlo toolkit*; Phys. Med. Biol. 66 244002 (2021)
- [38] E.E. Verwer et al., *Harmonisation of PET/CT contrast recovery performance for brain studies*; European Journal of Nucl. Medicine and Mol. Imaging 48, 8;2856-2870; 2021
- [39] One of the authors (HJF) observed non-detection by X-ray for four 90-year-old women who each spent a week in the hospital before a PET scan produced an unmmistakable diagnosis. You can calculate the efficiency from Poisson statistics yourself.
- [40] See S. Ritt, *The Role of Analog Bandwidth and S/N in Timing*, and J.-F. Genat, *Bandwidths of Transmission-Line Anodes* in Session 4; and D. Breton *Advanced Designs*, G. Drake *Dependence on Feature Size*, and E. Delagnes *Noise*, in Session 5 of the Workshop *The Factors that Limit Time Resolution in Photodetectors*, Univ. of Chicago; April 2011; https://psec.uchicago.edu/workshops/fast_timing_conf_2011/
- [41] For a far-seeing summary of the factors that determine time and space resolution in MCP-based detectors, see S. Ritt, *Overview of Limitations*; *ibid.*
- [42] Z. Insepov, V. Ivanov, S. J. Jokela, I. V. Veryovkin and A. V. Zinovev;
Comparison of secondary electron emission simulation to experiment;
Nucl. Instr. Meth A639, 155 (2011) This work was supported by the LAPPD Collaboration.